Recoil Nucleon Polarization in Deeply Virtual Compton Scattering and Neutral Pion Electroproduction in Hall C

(Dated: May 21, 2023)

We propose to use the Hall C DVCS experimental setup, consisting of the High Momentum Spectrometer to detect the scattered electron, the Neutral Particle Spectrometer to detect the photon, and a proton polarimeter made of scintillating fibers to measure the recoil nucleon polarization. At $Q^2 \sim 2$ GeV^2, a Bjorken-x scan will be performed with the polarized electron beam sent on a 15 cm-long unpolarized liquid hydrogen target. The recoil nucleon polarization in DVCS constrains both GPDs $\tilde{H}$ and E. The experimental setup will allow to simultaneously study exclusive π^0 electroproduction , giving more constrains on the chiral-odd GPDs.

M. Defurne[†], O. Bessidskaia Bylund,

DPhN (Saclay), CEA/DRF/IRFU, Gif-sur-Yvette, France

C. Muñoz Camacho,

Institut de Physique Nucleaire d'Orsay, IN2P3, BP 1, 91406 Orsay, France

A. Camsonne, B. Wojtsekhowski,

Thomas Jefferson National Accelerator Facility, Newport News, VA 23606, USA

[†] Contact person: `maxime.defurne@cea.fr`

Contents

I. INTRODUCTION

A. Introduction to GPDs and DVCS

Deeply Virtual Compton Scattering (DVCS) refers to the reaction $\gamma^* p \rightarrow p\gamma$ in the Bjorken limit of Deep Inelastic Scattering (DIS). Experimentally, we can access DVCS through electroproduction of real photons $ep \rightarrow ep\gamma$, where the DVCS amplitude interferes with the so-called Bethe-Heitler (BH) process. The BH contribution is calculable in QED since it corresponds to the emission of the photon by the incoming or the outgoing electron.
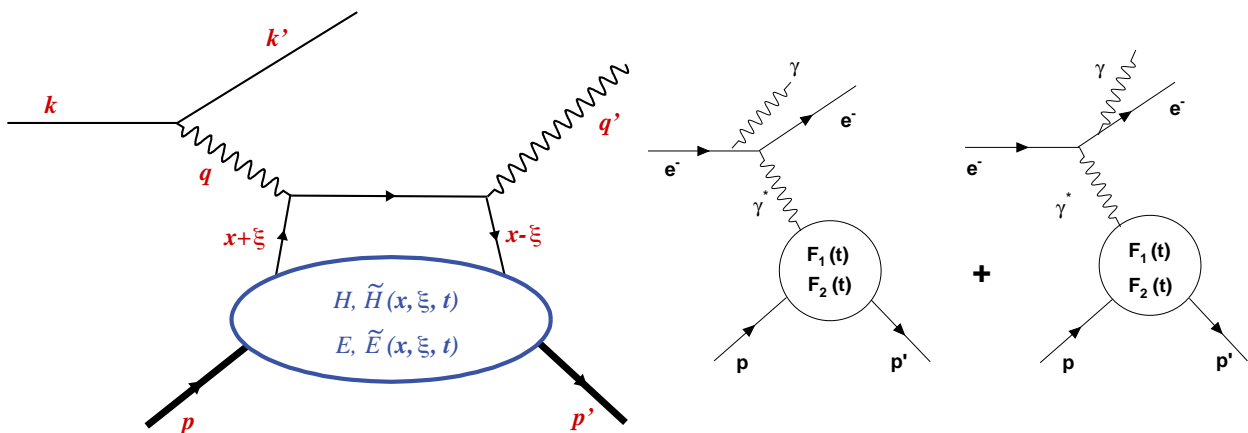

FIG. 1: Left: Leading-twist DVCS diagram at Leading-order. Right: Bethe-Heitler diagrams.

From the DVCS diagram presented in Figure 1, we can define several kinematical variables:

- $Q^2 = -|q|^2 = -|k-k'|$ is the virtuality of the process defined by the squared magntiude of the 4-momentum of the virtual photon.

- $x_B = \frac{Q^2}{2pq}$ is the Bjorken variable.

- t is the squared momentum transfer to the nucleon.

- ϕ_h is the angle between the leptonic plane, containing the leptons and the virtual photon, and the hadronic plane defined by the virtual photon, real photon and recoil proton.

DVCS is the simplest probe of a new class of light-cone (quark) matrix elements, called Generalized Parton Distributions (GPDs). The GPDs offer the exciting possibility of the first

ever spatial images of the quark waves inside the proton, as a function of their wavelength [1–6]. The correlation of transverse spatial and longitudinal momentum information contained in the GPDs provides a new tool to evaluate the contribution of quark orbital angular momentum to the proton spin.

GPDs enter the DVCS cross section through complex integrals, called Compton Form Factors (CFFs). CFFs are defined in terms of the vector GPDs H and E, and the axial vector GPDs $\tilde{H}$ and $\tilde{E}$. For example ($f \in \{u, d, s\}$) [7]:

$$\mathcal{H}(\xi, t) = \sum_f \left[\frac{e_f}{e}\right]^2 \left\{ i\pi \left[H_f(\xi, \xi, t) - H_f(-\xi, \xi, t) \right] \right.$$
$$\left. + \mathcal{P} \int_{-1}^{+1} dx \left[\frac{1}{\xi - x} - \frac{1}{\xi + x} \right] H_f(x, \xi, t) \right\}. \tag{1}$$

Thus, the imaginary part accesses GPDs along the line $x = \pm\xi$, whereas the real part probes GPD integrals over x. The 'diagonal' GPD, $H(\xi, \xi, t = \Delta^2)$ is not a positive-definite probability density, however it is a transition density with the momentum transfer $\Delta_\perp$ Fourier-conjugate to the transverse distance r between the active parton and the center-of-momentum of the spectator partons in the target [8]. Furthermore, the real part of the Compton Form Factor is determined by a dispersion integral over the diagonal $x = \pm\xi$ plus the D-term [9–12]:

$$\Re\left[\mathcal{H}(\xi, t)\right] = \int_{-1}^{1} dx \left\{ [H(x, x, t) + H(-x, x, t)] \left[\frac{1}{\xi - x} - \frac{1}{\xi + x} \right] + 2\frac{D(x, t)}{1 - x} \right\} \tag{2}$$

The D-term [13] only has support in the ERBL region $|x| < \xi$ in which the GPD is determined by $q\bar{q}$ exchange in the t-channel.

All CFFs parametreized the DVCS amplitude with different kinematical coefficients depending on the experimental conditions. Indeed, to disentangle the contributions of all CFFs, it is necessary to collect data with various combinations of beam and target polarizations as:

- beam-helicity dependent and independent cross sections for an unpolarized target are mostly sensitive to the real and imaginary parts of the CFF $\mathcal{H}$. The measurements performed by Hall A and CLAS collaborations with the upcoming Hall C experiments will provide strong experimental constrains in global fits for $\mathcal{H}$ over the entire phase space accessible with the 11 GeV beam..

- the CFF $\widetilde{\mathcal{H}}$ is constrained by observables collected with a longitudinally polarized target. Target spin asymmetries have been measured with CLAS. With CLAS12, data taking on a longitudinally polarized target just finished this spring 2023. The target-spin asymmetry constrains the imaginary part. Regarding the real part, the statistical accuracy of the double spin asymmetry (target and beam) must be small enough to significantly isolate a deviation from the large contribution of the Bethe-Heitler.

- observables collected with a transversely polarized target offer larger contributions of CFF $\mathcal{E}$ compared to unpolarized and longitudinally-polarized target. A run group proposal with CLAS12 was submitted with the idea of using a HD-ice target, supposed to hold the polarization long-enough under beam without magnetic field to take data. Recently this idea was abandoned and a conventional DNP target is considered at the possible cost of not detecting the recoil proton. Without detecting the recoil proton, the dilution factor increases significantly and dramatically reduce the figure-of-merit of such an experiment. Today there are no data collected with a transversely polarized target to constrain $\mathcal{E}$. Neutron DVCS offers an alternative solution to access $\mathcal{E}$ as the electromagnetic form factors in the DVCS/BH interference enhances its contribution even on unpolarized target. Therefore data has been naturally collected on deuterium target in Hall A and Hall B. Global fits of proton and neutron data are starting to consider these data at the cost of increasing the number of unknown with the flavor separation and assuming no final state interaction.

- Finally DVCS is poorly sensitive to $\widetilde{\mathcal{E}}$ and it is likely that it will be constrained with global fits using DVMP.

Nowadays, considering all the observables collected so far, global fits must still do assumptions and neglect one or two real/imaginary parts as the CFF extraction remains under-constrained. It is in the perspective of providing an alternative to a transversely polarized target and/or increasing the set of DVCS observables that the recoil nucleon polarization in DVCS is considered here as a new experimental DVCS observable. In this letter-of-intent, the sensitivity of this observable as well as a significance study with a Toy model of proton polarimeter is presented. Then a design of polarimeter is introduced as well as a study of the detector rates performed with Geant4. Finally a first performance study is realized with a preliminary tracking algorithm before discussing the remaining work to

be performed prior submission of a full proposal. A discussion about possible kinematical settings of interests as well as other measurement opportunities with the polarimeter will conclude this LOI.

B.   Introducing the recoil proton polarization in DVCS

The polarization axis in the lab frame are defined as follows for a fixed-target experiment:

- the y-axis is orthogonal to the hadronic plane and defined by $\gamma^*\gamma$,

- the z-axis is along the proton momentum in the lab frame,

- Finally the x-axis is in the hadronic plane, such as x-y-z is a right-handed system.

The polarization components are given by the ratio of an amplitude divided by the total cross-section. As any photon electroproduction observable, it can be decomposed into a beam-helicity independent P_i^u and a beam-helicity dependent part P_i^u for $i \in [x, y, z]$:

$$P_{x/z}^m = h_e \left(P_{x/z}^u + h_e P_{x/z}^h \right) \ , \tag{3}$$

$$P_y^m = P_y^u + h_e P_y^h \ . \tag{4}$$

With such a decomposition, the reader may notice that the beam-helicity dependent part is accessed by averaging over the helicity of the beam while the beam-helicity independent part is obtained by making the difference of the helicity states for x and z. It is the opposite for the y-component. Each term can be subsequently decomposed into a Bethe-Heitler, a DVCS and an interference contribution. Using Kroll-Goloskokov model, these contributions are plotted as function of ϕ_h in Figure 2, decomposing only the amplitude at the numerator and keeping all terms at the denominator in the cross section. Therefore, the predicted polarization is easily recovered by adding the BH, DVCS and interference contributions. As any DVCS observable, the contribution of the different terms are changing much with ϕ_h. There are three main conclusions to draw from Figure 2:

- As being a radiative elastic scattering process, Bethe-Heitler induces polarization along x- and z-components but almost none along the y-axis. The y-component is therefore a quasi-pure CFF information.

- Regarding the beam-helicity dependent polarizations, they are almost pure interference with a *sinusoidal* shape reaching its maximum between 45 and 90 degrees. It is small for the y-component as the Bethe-Heitler amplitude is almost 0. But its amplitude for x- and z-components is as large as the beam-helicity independent term.

- The Bethe-Heitler term at the denominator rapidly increases at the denominator when getting to small ϕ_h, suppressing dramatically the interference and DVCS induced polarization. As the total amplitudes of BH, DVCS and interference amplitude are more balanced between 90 and 270 degrees, interference and DVCS contribution become sizable.
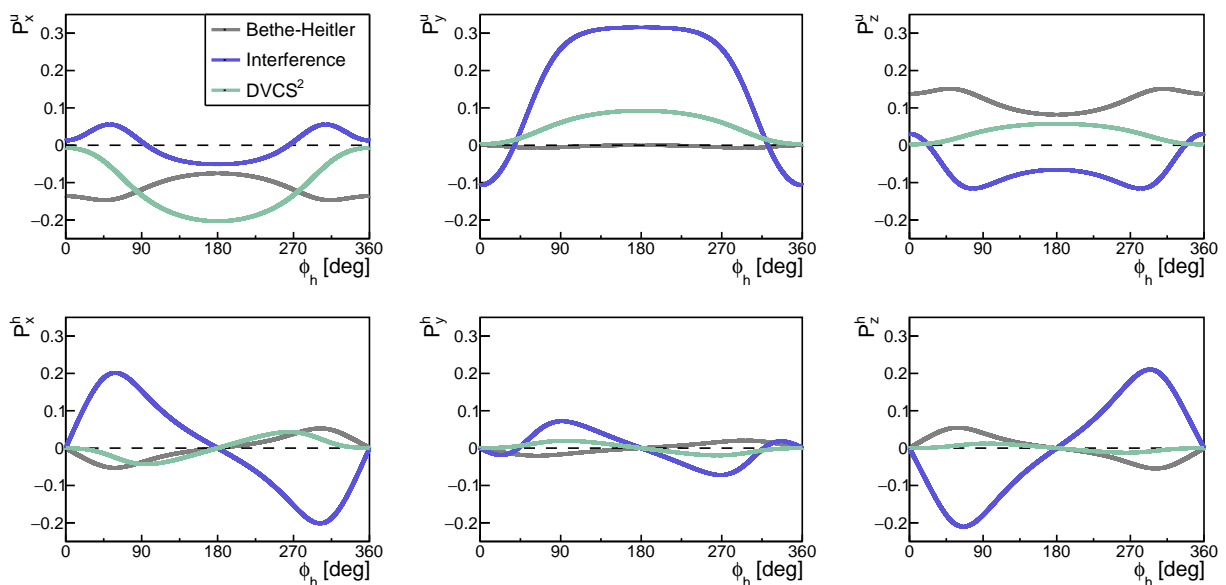

FIG. 2: Bethe-Heitler, DVCS and interference contributions to the beam-helicity independent and dependent polarization terms.

To highlight the CFF sensitivity, we consider the first-order derivatives with respect to imaginary and real parts of CFFs: this quantity is not as biased by the model as a simple prediction. The derivatives depend very much on ϕ_h. For all components, the sensitivity to $\widetilde{\mathcal{E}}$ is almost none as mentionned in the introduction. It does not mean that $\widetilde{\mathcal{E}}$ is not contributing at all but that it must be one or two order of magnitudes larger than the other CFFs to contribute as well. The x-component is particularly sensitive to the real part of $\widetilde{\mathcal{H}}$ at $\phi_h=180°$ for the beam-helicity independent part whereas the imaginary part

almost completely governs the beam-helicity dependent term. Similar conclusions hold for P_z although the sensitivity is slightly reduced. Regarding P_y, it offers an equal sensitivity to $\mathrm{Im}\mathcal{H}$, $\mathrm{Im}\widetilde{\mathcal{H}}$ and most interestingly to $\mathrm{Im}\mathcal{E}$ at ϕ_h=180 degrees. In a global fit of cross sections and both P_x with P_y, all three CFFs (both real and imaginary parts) will be disentangled.
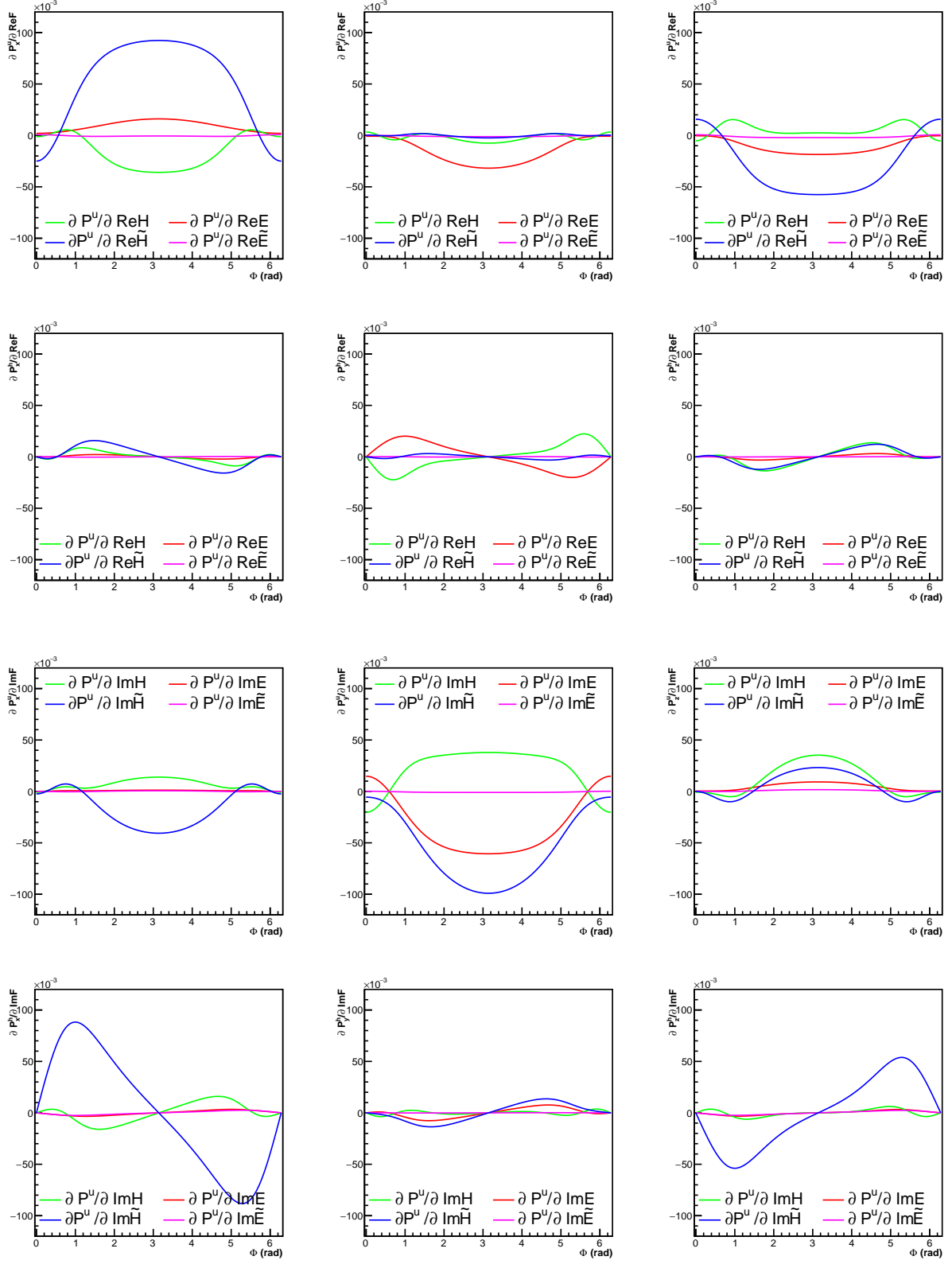
FIG. 3: Partial derivative with respect to imaginary or real part of each CFFs. The first column is for P_x, the second for P_y and the third for P_z.

II.   PHYSICS GOALS

The physics goal is to measure the beam-helicity independent polarization terms for x- and y-components for a DVCS recoil proton in the Hall C of Jefferson Lab. When possible (*i.e.* ϕ_h between 45 and 90 degrees), beam-helicity dependent terms will also be extracted. The scattered electron would be detected in the High Momentum Spectrometer whereas the photon is detected by the Neutral Particle Spectrometer. The recoil proton will be analyzed in a polarimeter not exisiting yet. First, we are going to briefly remind the reader about proton polarimetry. Then we will present a design of polarimeter, the detector rates and a preliminary study of its performance with Geant4.

A.   Introduction to proton polarimetry

Due to the spin-orbit coupling, when transversally polarized protons strike a nucleus N, an azimuthal dependence in the pN-cross section will be induced. Exploiting this effect, one can measure the average polarization of a set of protons in a statistical measurement. A proton polarimeter is therefore constituted of an analyzer off which the protons will scatter, surrounded by a set of trackers upstream and downstream the analyzer to determine the polar θ_{pol} and azimuthal ϕ_{pol} scattering angles in the polarimeter as illustrated by Figure 4.
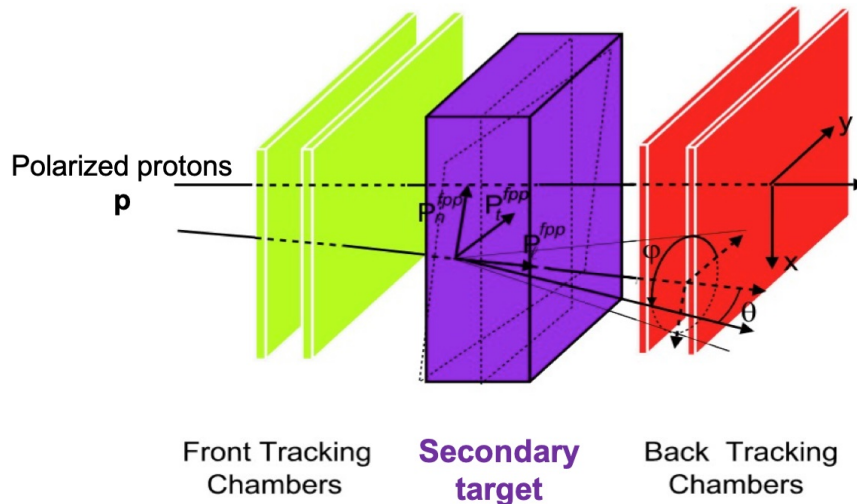

FIG. 4: Schematic of a polarimeter. In this figure, θ is θ_{pol} in the text, same for ϕ being ϕ_{pol} in the text.

To define θ_{pol} and ϕ_{pol} , we are following the convention found in [21] with x- and y-directions defined as explained in the previous section. With $\mathbf{p}'$ being the incoming proton momentum and $\mathbf{p}_{pol}$ the rescattered proton momentum, the normal vector $\hat{\mathbf{n}}$ is defined as:

$$\hat{\mathbf{n}} = \mathbf{p}' \times \mathbf{p}_{pol}/|\mathbf{p}' \times \mathbf{p}_{pol}| \qquad (5)$$

The scattering angles are then given by

$$\sin\theta_{pol} = |\mathbf{p}' \times \mathbf{p}_{pol}| \,,$$
$$\sin\phi_{pol} = -\hat{\mathbf{x}} \cdot \hat{\mathbf{n}} \,, \quad \cos\phi_{pol} = \hat{\mathbf{y}} \cdot \hat{\mathbf{n}} \,. \qquad (6)$$

The following distribution is then observed:

$$\frac{dN}{d\theta_{pol}} = N_0 \cdot \frac{d\epsilon}{d\theta_{pol}} \cdot (1 + A_p(P_y \cos\phi_{pol} - P_x \sin\phi_{pol})) \,. \qquad (7)$$

with N_0 is the total number of incident protons, $\frac{d\epsilon}{d\theta_{pol}}$ and A_p the differential efficiency and the analyzing power of the polarimeter and P_x, P_y being the transverse polarizations to the proton momentum. The analyzing power gives the sensitivity of the scattering process to the proton polarization. In this work we are considering a Carbon analyzer with density 1.7g/cm^3.

Both the efficiency and the analyzing power depend on the polar scattering angle θ_{pol} and on the incoming proton momentum at the center of the analyzer. The efficiency [20] is also function of the analyzer thickness - the longer it gets, the higher the number of target nuclei to rescatter off. Two different parametrizations of the analyzing power are available in McNaughton's [19] paper for the momentum range of interest for this work, a low-energy and high-energy parametrization for kinetic energies at the center of the analyzer up to 450 MeV and 750 MeV respectively. The figure of merit [20] for a polarimeter can be characterized as:

$$F_p^2 = \int_{\theta_{min}}^{\theta_{max}} A_p(\theta_{pol})^2 \epsilon(\theta_{pol}) \mathrm{d}\theta_{pol} \,. \qquad (8)$$

In our calculations, the efficiency and analyzing power are integrated over the range of 4-19 degreses in θ_{pol}.

In Fig. 5 a scan of the analyzing power, efficiency and figure of merit as a function of proton kinetic energy at the center of a Carbon analyzer T_{carb} is shown. While the efficiency increases with kinetic energy, the analyzing power is the largest around $T_{carb} = 200$ MeV and the figure of merit for the polarimeter peaks between 200 and 300 MeV.
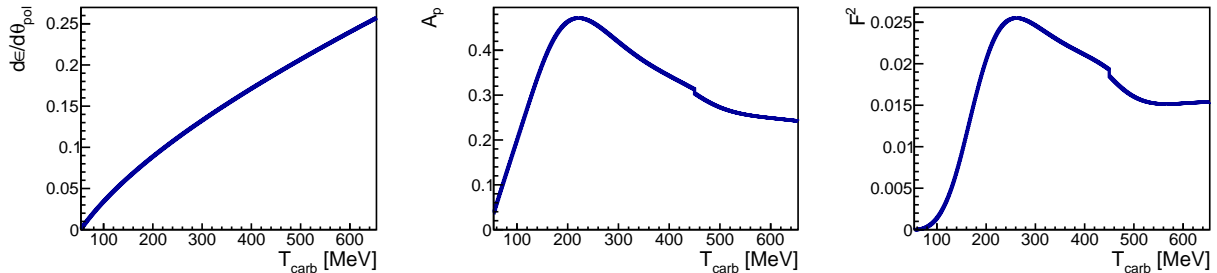
FIG. 5: A scan over differential efficiency (left), analyzing power (center), and F^2 (right) as a function of the kinetic energy in the center of the analyzer. The shown range corresponds to a proton momentum of 320-1290 MeV/c at the center of the analyzer.

In Fig. 6, the analyzing power and efficiency are shown as a function of the scattering angle θ_{pol} for three different proton energies. The efficiency is seen to drop with θ_{pol}, while the general shape on the analyzing power varies with the proton energy.
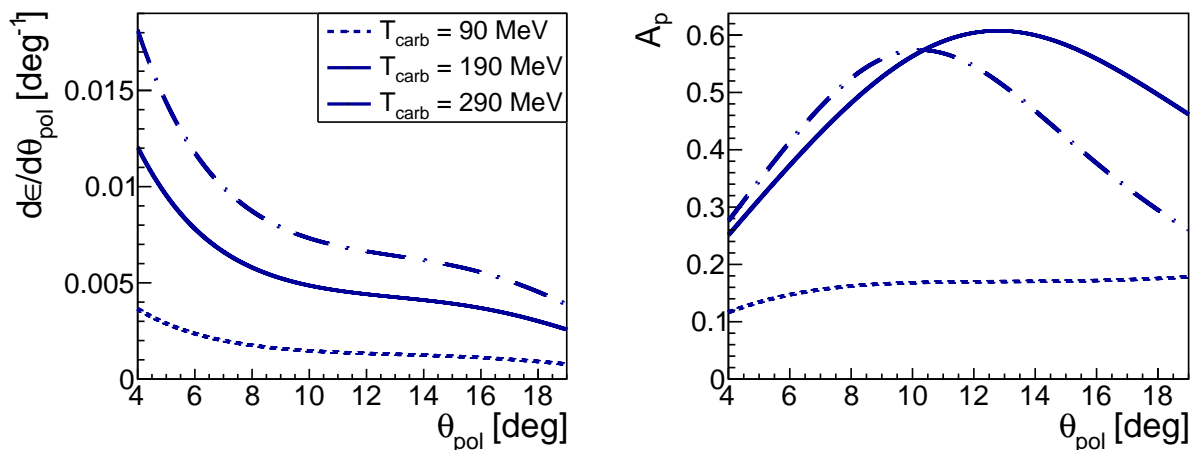

FIG. 6: The differential efficiency (left) and analyzing power (right) as a function of θ_{pol} for a proton with kinetic energies of 90 MeV, 190 MeV and 290 MeV at the center of the carbon analyzer.

The statistical error on the measured polarization is proportional to:

$$\delta_P \propto \frac{1}{F\sqrt{N_{inc}}} \,, \tag{9}$$

with N_{inc} denoting the number of incident protons.

B. Finding suitable kinematic settings

From the study of the CFF sensitivity, we already know that it is better to perform a measurement with ϕ_h between 90 and 270 degrees to constrain $\widetilde{\mathcal{H}}$ and $\mathcal{E}$. As a longitudinally polarized target experimental program has already been carried out with CLAS12, our focus is the elusive CFF $\mathcal{E}$ as no DVCS measurement with a transversely polarized target has ever been carried out at Jefferson Lab. The CFF $\mathcal{E}$ is only accessible through the orthogonal direction to the hadronic plane: Unlike elastic scattering, spin precession is not necessary and must be carefully considered here for the polarimeter design as it would simply blur the sensitivity of the measurement to the CFF $\mathcal{E}$.

However constraining the CFF $\mathcal{E}$ does not only depend on the polarization sensitivity but also on the number of incoming protons and the analyzing power/efficiency of the polarimeter being functions of the kinetic energy of the proton. In other words, the statistical accuracy of the polarization measurements strongly depends on the kinematics as well. To find a suitable kinematic settings, the maximum of the following figure-of-merit was searched over a 5D grid of kinematics formed by the beam energy, Q^2, x_B, t and ϕ_h:

$$\mathcal{F} = \sqrt{\frac{d\sigma}{dQ^2 dx_B dt d\phi_h}} \times F_p \times \left| \frac{\partial P_y}{\partial Im\mathcal{E}} \right| , \tag{10}$$

with $\frac{d\sigma}{dQ^2 dx_B dt d\phi_h}$ the photon electroproduction cross section, F_p the figure-of-merit of the polarimeter and $\left| \frac{\partial P_y}{\partial Im\mathcal{E}} \right|$ the derivative of P_y with respect to imaginary part of $\mathcal{E}$. In addition, it was required that the angle between all particles in the final state and the beam is above $10°$. Finally, we required $t/Q^2 <= 0.25$. It lead to the kinematics shown before, *i.e.* E=10.6 GeV, Q^2=1.8 GeV^2, x$_B$=0.17, t=-0.45 GeV^2 and ϕ_h=180° with a beam energy at 10.6 GeV. The table I summarizes the angles and momenta of the different particles.

	electron $|k'|$	$\theta_{k'}$	photon $|q'|$	$\theta_{q'}$	proton $|p'|$	$\theta_{p'}$
Kin1	4.96 GeV/c	10.6°	5.40 GeV/c	-15.1°	0.71 GeV/c	44°

TABLE I: Particle angles and momenta for Kin1. Particles with angles sharing same sign are on the same side of the beam.

A local expression of the numerator amplitudes for P$_x$ and P_y at Kin1 are given by

Equations 11 12. The constant term is the Bethe-Heitler contributions. The linear part in CFF is the BH/DVCS interference term and the bilinear part is the DVCS amplitude. These expressions are not model-dependent unlike the partial-derivative plots and provide more details. For instance, the partial derivative of P_y^u with respect to $\mathrm{Im}\widetilde{\mathcal{H}}$ indicates a strong sensitivity to the latter that does not arise from interference but fom the bilinear combinations with $\widetilde{\mathcal{E}}$.

$$
\begin{aligned}
\mathcal{M}^m(x) = {} & -20.42 + 19.06\ \mathrm{Re}\tilde{\mathcal{H}} + 7.15\ \mathrm{Re}\mathcal{H} - 1.04\ \mathrm{Re}\mathcal{E} - 0.56\ \mathrm{Re}\tilde{\mathcal{E}} \\
& -2.93\left(\mathcal{H}\tilde{\mathcal{H}}^* + \mathcal{H}^*\tilde{\mathcal{H}}\right) + 0.16\left(\mathcal{E}\tilde{\mathcal{H}}^* + \mathcal{E}^*\tilde{\mathcal{H}}\right) \\
& +0.04\left(\mathcal{H}\tilde{\mathcal{E}}^* + \mathcal{H}^*\tilde{\mathcal{E}}\right) + 0.03\left(\mathcal{E}\tilde{\mathcal{E}}^* + \mathcal{E}^*\tilde{\mathcal{E}}\right)
\end{aligned}
\tag{11}
$$

$$
\begin{aligned}
\mathcal{M}^m(y) = {} & 15.50\ \mathrm{Im}\mathcal{H} - 10.05\ \mathrm{Im}\mathcal{E} + 3.44\ \mathrm{Im}\tilde{\mathcal{H}} - 0.44\ \mathrm{Im}\tilde{\mathcal{E}} \\
& +1.51\ \mathrm{Im}\left(\mathcal{E}\mathcal{H}^* - \mathcal{E}^*\mathcal{H}\right) + 0.14\ \mathrm{Im}\left(\tilde{\mathcal{E}}\tilde{\mathcal{H}}^* - \tilde{\mathcal{E}}^*\tilde{\mathcal{H}}\right)
\end{aligned}
\tag{12}
$$

To have a first estimate of the measurement accuracy and its significance with respect to model prediction, a Toy Monte-Carlo simulation was performed in [14]. The Geant4 simulation of the Hall C experimental setup was used. The polarimeter was not implemented for the predictions in the article but parametrizations of analysing power and efficiency were used as weights, assuming a 15-cm thick graphite analyzer, when the proton was emitted within a 40 degrees * 60 degrees window around the center of the polarimeter. Assuming a 10 μA beam sent on a 15cm-long liquid hydrogen target for 3 weeks and an ideal tracking system for the polarimeter, we obtained the Figure 7 representing the azimuthal distributions summed or subtracted over the beam helicity. As the reader can see, the measurement would strongly discriminate between the various model predictions. Using a reweighting technique for the PARTONS global fit using neural networks, we determined that the measurement would reject 90% of the ANN replicas, demonstrating the significance of the measurement.

From these distributions, an average analyzing power of 0.3 and efficiency of 10% were estimated.
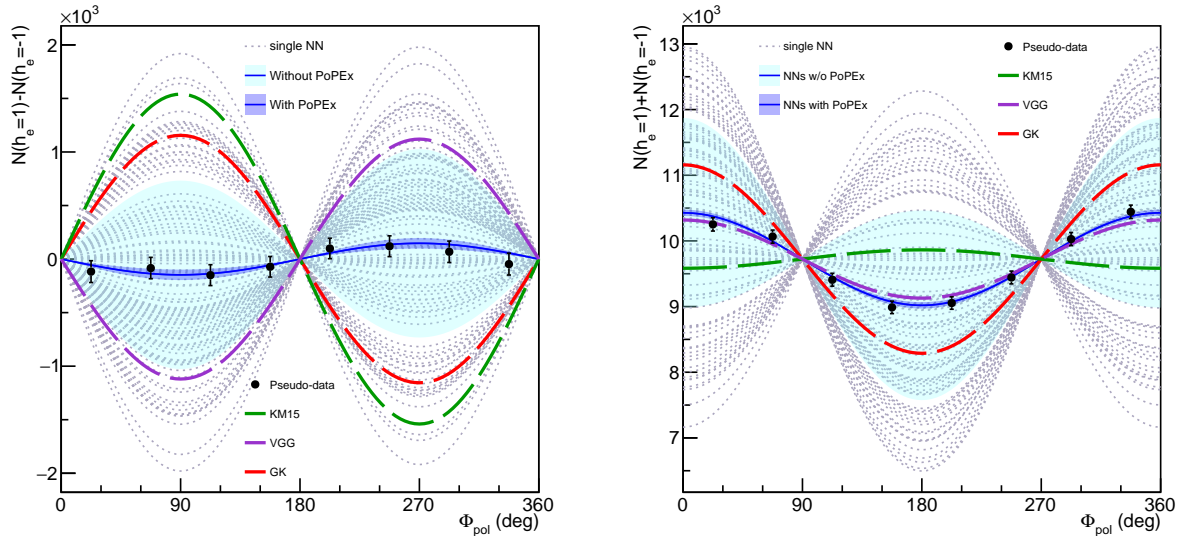
FIG. 7: Estimated azimuthal distributions of rescattering events in [14]. Predictions for various GPD/CFF fits are also displayed: Green curve for KM15, red for GK, purple for VGG and blue for PARTONS used here as a reference. The dark blue band represents the fit uncertainty of the distribution, considering only statistical uncertainty, to be compared with the light blue band.

C. Concept of the proton polarimeter

In a first attempt, we would like to avoid using magnetic fields to clear the background as it would induce spin precession. Therefore the polarimeter will have a direct sight on the target and must cope with the background rate. As DVCS is an exclusive process, the recoil proton momentum can be inferred from the photon and scattered electron. Both position and timing of the proton can be used given a small-enough segmentation and a fast-enough detector. Such specifications can be achieved by scintillating fibers as it is explained in the next subsection. Then a polarimeter design will be described. Finally detector rates and a preliminary assessment of the polarimeter performances will be presented.

1. Scintillating fibers

The light yield of a scintillating material primarly depends on the energy deposited by ionization. The thinner the material is, the fewer the photons are. Although scintillating materials are amongst the first particle detectors being ever used, their size were limited by the

light yield. With the progress made on the cladding technology and high quantum-efficient light detectors such as Silicon Multipliers, scintillating fibers became a reality. Figure 8 dis-
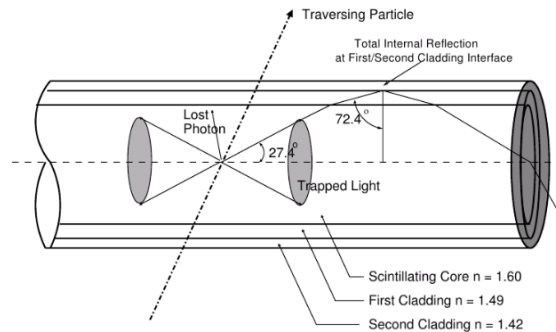

FIG. 8: Schematic of a scintillating fiber.

plays the schematic of a multicladding scintillating fiber: a charged particle ionizes the core made of polystyrene, isotropically emitting photons with a wavelength between 400-600nm. Thanks to the reflection at the interfaces between the various materials, a large-enough fraction of light is trapped to be detected at the end of the fiber. Here are a few numbers regarding scintillating fibers [15].

- 8000 photons are produced per MeV deposited in the fiber material. For information a MIP deposits 2 MeV/cm in polystyrene.

- For a multicladding fibers, the fraction of trapped photons emitted in a single hemi-sphere is about 5%.

- By applying a reflective coating on the other extremity of the fiber, it is possible to increase by 70% the light yield.

- Typical absorption length ranges from 3 to 4 m.

As previously mentionned, the development of Silicon Photo-Multipliers (SiPMs) with quantum-efficiency peaking as high as 40% have allowed to use the scintillating fiber technology to build large scale detectors such as The Sci-Fi LHCb tracker [15] and the HERMES recoil detector [16] for tracking, or the scintillating fiber timing detector for the mu3e experiment [17]. For the latter, a time resolutions of 250ps is achieved. Finally an active fiber target (AFT) [18] is being assembled to study Ξ-hypernucleus at J-PARC. A prototype was

successfully tested and the full-scale detector is being assembled. By its design and purpose, this detector is close to the polarimeter described in the next section.

2.   *Polarimeter design*

As described in Figure 9, the polarimeter has a trapezoidal shape. Along the depth of the trapezoid being the path of the recoil proton at the central kinematics, the following pattern is repeated 15 times: 5 consecutive layers of horizontal fibers, then 5 layers of vertical fibers and 5mm of graphite to add analyzing material and therefore increase the efficiency of the polarimeter. The current diameter of the fiber is 1 mm. Consequently the total depth is approximately 21 cm. The upstream face is 40 cm wide and 60 cm high, while the downstream face is 80 cm wide and 100 cm high. This enlargement allows to keep an optimal azimuthal acceptance for recoil proton entering the polarimeter on the edges of the front face.

Four shields of 2.6 cm-thick graphite covers the front, the bottom and the closest wing
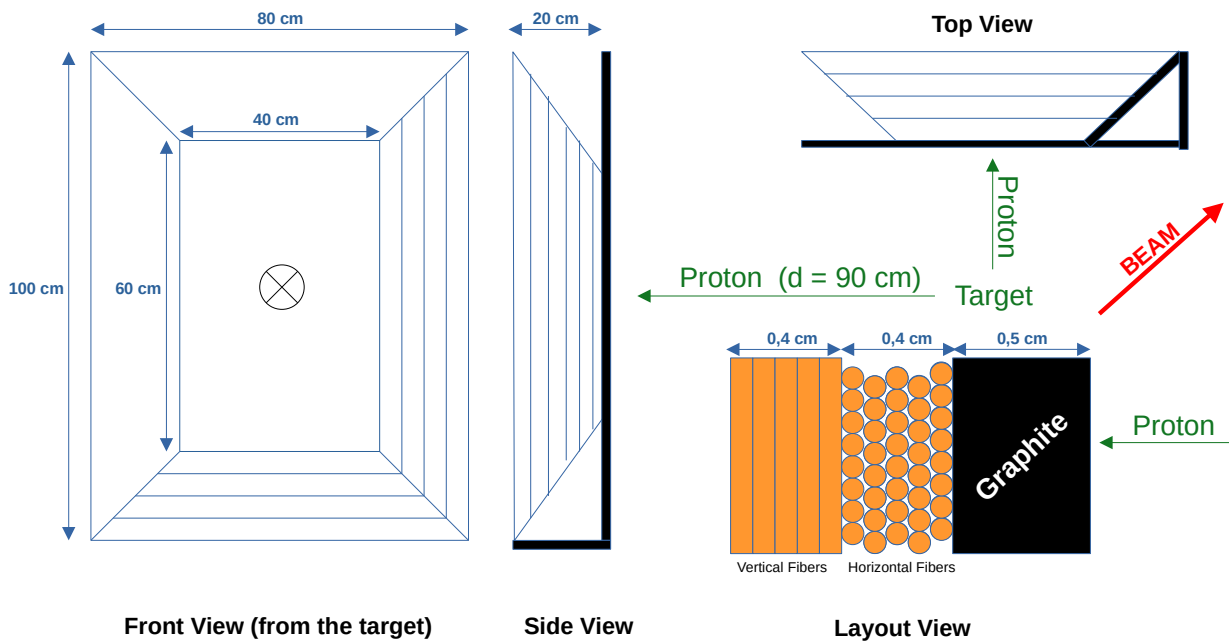

FIG. 9: Schematic of the polarimeter.

of the polarimeter to the beam. It allows to suppress Moller electrons with energy below 10 MeV for the front face, and 25 MeV for the wing. The front shield may increase as well

the efficiency of the polarimeter if we consider that the incident recoil proton trajectory is gien by the scattered electron and photon.

D. Detector rates and performances

1. Detector rates

In order to get a preliminary assessment of the detector rates, a Geant4 simulation has been run by sending 10.6 GeV electron through the 15cm-long liquid hydrogen target including its aluminium window with the previously described geometry for the polarimeter. In Figure II D 1, rates for vertical (Y-) fibers and horizontal (X-) fibers are presented. Energy deposit in the fibers were saved and a number of photons was randomly generated for each fiber based on the specifications introduced in subsection II C 1.

For the vertical fibers closest to the beam and the target, the rates go up to 3 MHz/μA. Assuming a 6 ns time window to find the proton (corresponding to a 3σ-window if the time resolution is only of 1 ns), these high-rate fibers have 12.6%-chance to be lit within the proton window for a 7μA-beam and the integrated occupancy of this first layer would be of 6%. If we consider the constrains on the recoil proton momentum from the scattered electron and the photon, it seems likely that the proton detection and tracking would not suffer too much at this occupancy. Along the beam side/wing of the polarimeter, rates of vertical fibers may go up to 6 MHz/μA. But as the purpose of this wing is to only follow the rescattered proton and not to detect the incoming protons, we may be able to tolerate a higher background rate. Further studies are required to caracterize the background, optimize a tracking algorithm and produce "the-occupancy-against-the-tracking-efficiency" to find the maximum beam current.

Regarding horizontal layers, the rates are significantly lower with a maximum of 1.4 MHz/μA on the very first layer of fibers.

2. Polarimeter performance

Using a set of modified Geant4 classes to include nucleon-nucleus polarized scattering, 10 000 protons were sent from the target through the center of the polarimeter, with a
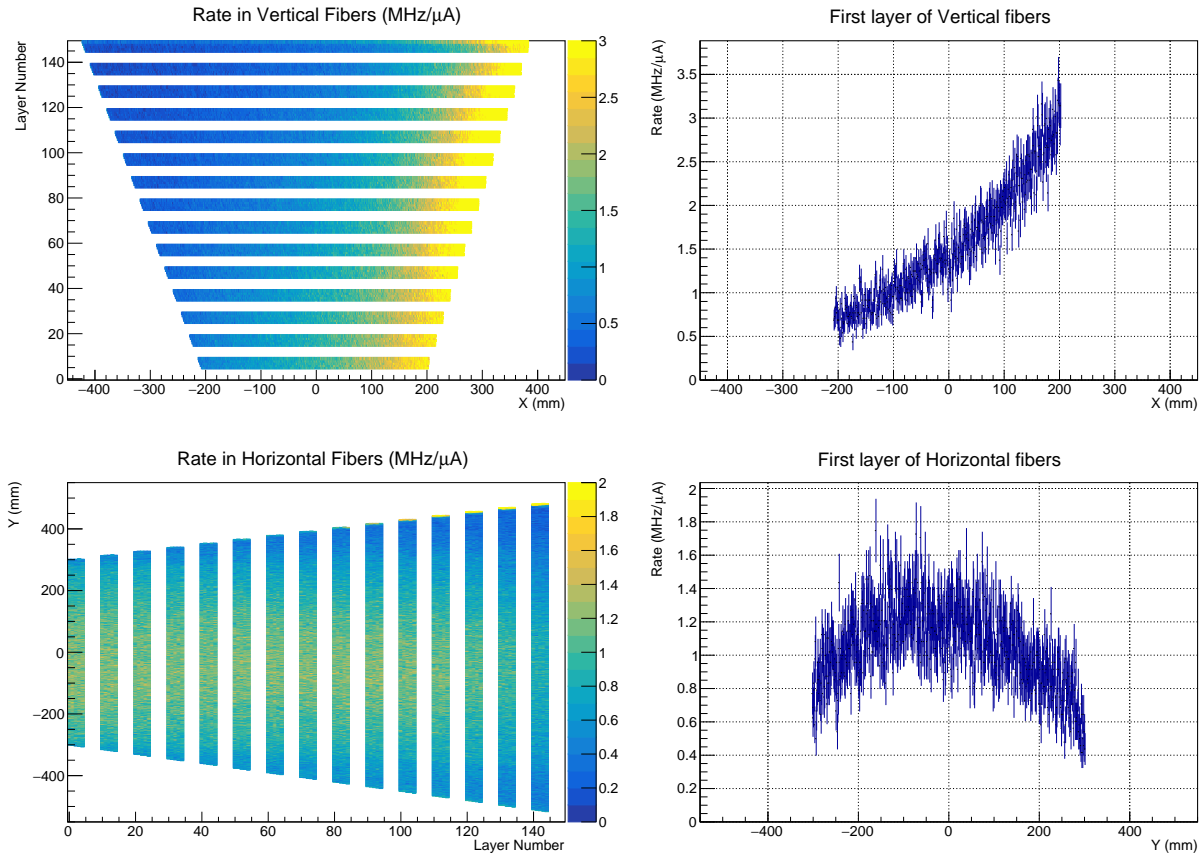
Top row: Rates expressed in MHz/μA for the vertical fibers as function of the layer depth (left) and for the closest layer from the target (right). Bottom row: Rates expressed in MHz/μA for the horizontal fibers as function of the layer depth (left) and for the closest layer from the target (right).

100% polarization along Y with a momentum of 700 MeV/c. Three examples of events are displayed in Figure 10.

From the knowledge of the generated momentum, we can compare the predicted position of the proton at the first fiber layer and the measured position to determine the effect of multiple scattering between the target and the scintillating fibers. As seen on Figure 11, the standard deviation of both residuals on horizontal and vertical fibers are about 2 mm. The final resolution for the experiment will entangle the resolutions of the HMS and NPS as they will provide the vertex and recoil proton momentum information.

Both set of fibers are first analyzed independently. First we must identify the beginning of the track corresponding to the incoming recoil DVCS proton in both X and Y directions. If no significant scattering place is found on both directions, the events is discarded. If a
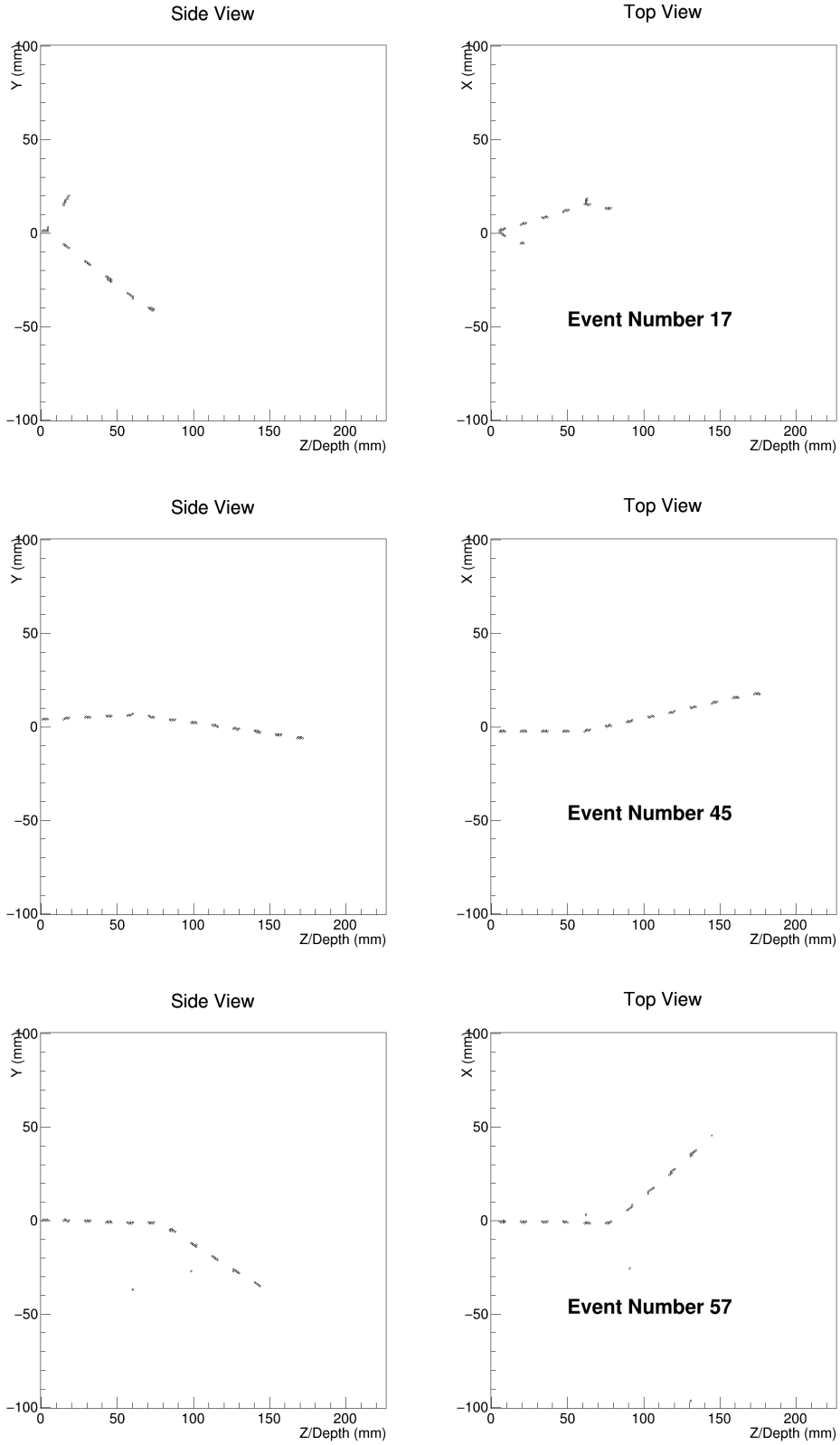
FIG. 10: Each row is a different event display. Left column shows side views of the poalrimeter and the right one shows top views.
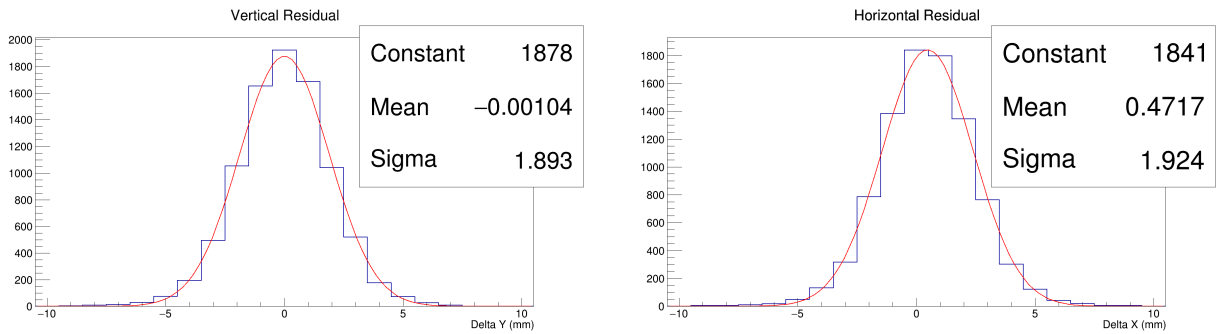
FIG. 11: left: Residual for the first plane of horizontal fibers. Right: same for vertical fibers.

rescattering event is spotted in one plane, it triggers a refined analysis of both planes around the presumed location of the rescattering event. This refined analysis allows sometimes to spot small angles in the plane none was found in a first place and/or reduce the effect of multiple scattering as the angle is determined from a tracking performed within 4.5cm upstream/downstream of the rescattering place. When a vertex can be found in each direction, we can compare their location displayed by Figure 12.
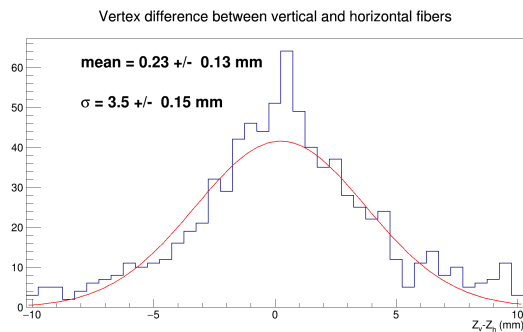

FIG. 12: Difference in the z-coordinate (depth in the polarimeter) of the rescattering place from the Y- and the X-analysis

For polarization analysis, we consider rescattering polar angle θ_{pol} between 5 and 40 degrees. In Figure II D 2, we have studied azimuthal angle (ϕ_{pol}) distributions as a function of the polar angle of the rescattering event (θ_{pol}) to estimate the average efficiency and analyzing power, knowing that the proton was fully polarized along Y. The efficiency and the analyzing power were derived by fitting the distributions with the following function:

$$N(\phi_{pol}) = N_0 \times \epsilon \times (1 + A_p \cos \Phi_{pol}) \ , \tag{13}$$

where N_0 is the number of incident protons (10000 here), ϵ the efficiency and A_p the analyzing

power. As expected, the efficiency decreases with the polar angle of the rescattering process. The analyzing power is found to be maximal for θ_{pol} between 8 and 11 degrees with $A_p = 0.342 \pm 0.08$.
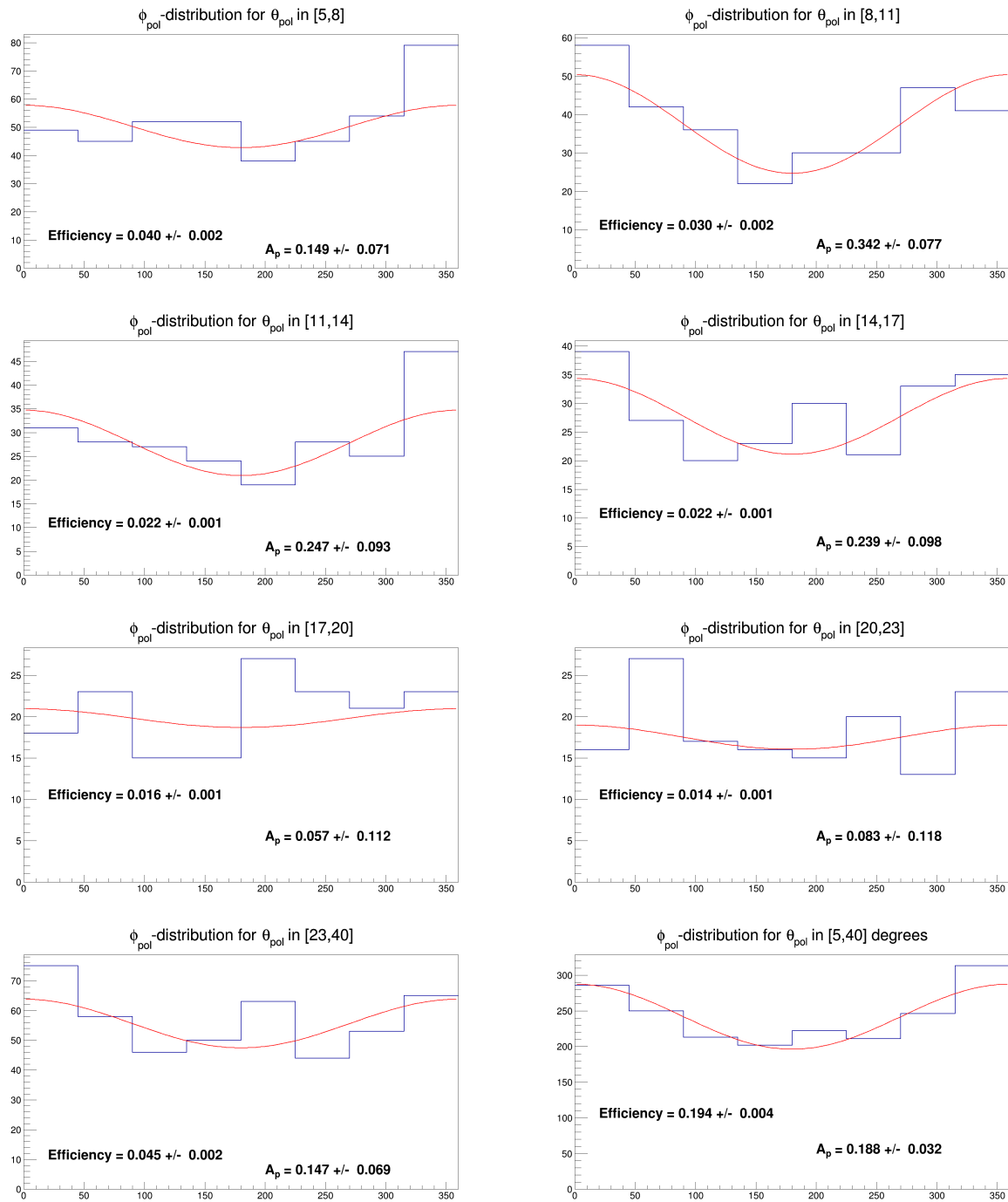
From top left to bottom right, azimuthal distributions of rescattering events for various polar angle θ_{pol}. The bottom right plot is the sum of all previous plots.

Integrated over the polar angle from 5 to 40 degrees, we found a global efficiency of

20% and an average analyzing power of 0.2. As it is with a first implemetation of tracking algorithm, we can consider these numbers as a lower bound of the polarimeter performances. The "lower-bound" figure-of-merit is very close to the one derived with the Toy MC and published in [14].

III.   DISCUSSION-CONCLUSION

A.   Limits of the approach

1.   Validity of the polarimetry parametrizations

Here with the scintillating fibers, events can be studied even if the proton does not exit the analyzer. It raises the question of the parametrization validity for the analyzing power as they were usually derived with passive analyzer in which protons were stopped or undergone multiple scattering all along their path. A calibration of the polarimeter might be necessary to derive the most appropriate analyzing power parametrization as it will most likely represent the main systematic uncertainty.

2.   Tracking algorithm

Only a simple pattern recognition and tracking algorithm were implemented. But it makes no doubt that a Machine Learning algorithm will be more efficient and accurate in analyzing the events. For sure it will offer the best resilience against the background rate and may allow us to run with a beam current of $10\mu A$ or higher. Our goal is to finalize the proposal using a properly trained Machine-Learning algorithm.

3.   Design of the polarimeter

The Pattern recognition/Tracking algorithm must also be well advanced to assess the DAQ requirements. For the studies shown in this letter, we assumed each fiber read independently. As the present design is composed of approximately 105 000 fibers, the read-out/DAQ cost will be expensive. Within the limit defined by the Proton Finding-Tracking algorithm efficiency and the detector rates, we will optimize the read-out/DAQ system to

reduce the cost.

Finally we do not exclude to replace 2 layers of each 5-layer group of 1mm-diameter fibers with 4 layers of 0.5mm-diameter fibers if the resolution for small-angle rescattering events is not sufficient.

B. x_B-scan

Two other kinematical settings will be considered in the preparation of the proposal to perform a x_B-scan. They are listed in Table II with Kin1.

	E_b (GeV)	$Q^2(GeV^2)$	x_B	t (GeV^2)	ϕ_h	$d^4\sigma$ (pb/GeV^4)
Kin 1	10.6	1.8	0.17	-0.45	180	27.8
Kin 2	10.6	2	0.25	-0.4	90	29.8
Kin 3	6.6	2	0.32	-0.4	90	33.1

TABLE II: Tables summarizing the kinematics. The last column gives the cross section with KM15.

Unlike Kin1, ϕ_h for the other proposed kinematics is 90 degrees. Indeed, for ϕ_h=180 degrees, all particles are in the horizontal plane. By imposing a minimal angle between all particles, including the beam, the phase space reduces almost to Kin1 for ϕ_h=180 degrees. Although the sensitivity to E is slighty smaller at 90 degrees, we benefit from a higher cross section compensating for the sensitivity loss and we can measure the beam-helicity dependent term of P_x strongly constraining Im$\widetilde{\mathcal{H}}$.

However, at ϕ_h=90 degrees, the photon and the recoil proton are in the same vertical plane. Consequently these two kinematical settings can only be studied without sweeping magnet. Additional simulations will be performed to ensure detector rates and accumulated dose are under control for NPS without sweeping magnet.

C.   Nucleon polarimetry for exclusive processes

Previously we focused on proton DVCS. But, as the title of the LOI indicates, we can consider neutron exclusive processes as well. For almost free, the polarization measurement

would be a side-product of tagging the neutron in the scintillating fibers by the detection/tracking of the secondary recoil proton. The measurement would be more delicate though as only the secondary recoil proton from the rescattering event in the fiber would be seen. The track of the secondary recoil proton would start around the expected trajectory of the neutron derived from the scattered electron and the photon at the expected coincidence time. Once a design has been finalized for the proton DVCS, we are going to assess its performance for neutron tagging and polarimetry. We already consider swapping the graphite layers with polyethylene to increase the proton content of the polarimeter.

Not only DVCS would benefit from such a polarimeter, but the DVCS experimental setup is also able to measure π^0-electroproduction as well. Peter Kroll has been contacted and is currently computing the recoil proton polarization for pion electroproduction.

D. Conclusion

In this letter-of-intent, we declare our intent to design an experiment able to measure the recoil proton and neutron polarization for DVCS and π^0-electroproduction using the High Momentum spectrometer of Hall C, the neutral particle spectrometer and a active polarimeter made of scintillating fibers to be designed. It was demonstrated that both CFFs $\mathcal{E}$ and $\widetilde{\mathcal{H}}$ will be constrained with this measurement. We have described a preliminary design that has been implemented in Geant4 and is currently being caracterized. Preliminary results regarding efficiency and analyzing power (currently underestimated) are compatible with numbers published in [14] and gives an equivalent figure-of-merit. In this article, it was quoted a beamtime estimate of 3 weeks at 10μA on a 15cm-long LH$_2$ target. To finalize a beamtime request for proton measurements, more work is required to refine the polarimeter design and improve the tracking algorithm. However, if by improving the tracking, the average estimated analyzing power increases from 0.2 to 0.3 as in [14], then 10 PAC days per kinematics should be enough as we have a much higher efficiency than in [14] by detecting protons stopping in the analyzer. Regarding the neutron observables, more work will be required on the tracking algorithm to determine if the same detector (replacing nevertheless the graphite layers with CH$_2$) could be used as well.

By submitting this letter, we are looking for PAC endorsement as well as feedback on the

proposed experiment. Any advice, recommendation or point of concern given by the PAC will for sure increase the quality of the proposal that we hope to submit next year.

REFERENCES

[1] D. Mueller, D. Robaschik, B. Geyer, F. M. Dittes, and J. Horejsi, Fortschr. Phys. **42**, 101 (1994), hep-ph/9812448.

[2] X.-D. Ji, Phys.Rev. **D55**, 7114 (1997), hep-ph/9609381.

[3] X.-D. Ji, Phys. Rev. Lett. **78**, 610 (1997), hep-ph/9603249.

[4] X.-D. Ji, W. Melnitchouk, and X. Song, Phys.Rev. **D56**, 5511 (1997), hep-ph/9702379.

[5] A. V. Radyushkin, Phys. Rev. **D56**, 5524 (1997), hep-ph/9704207.

[6] A. Radyushkin, Phys.Lett. **B380**, 417 (1996), hep-ph/9604317.

[7] A. V. Belitsky, D. Mueller, and A. Kirchner, Nucl. Phys. **B629**, 323 (2002), hep-ph/0112108.

[8] M. Burkardt (2007), 0711.1881.

[9] O. Teryaev (2005), hep-ph/0510031.

[10] I. Anikin and O. Teryaev, Phys.Rev. **D76**, 056007 (2007), 0704.2185.

[11] I. Anikin and O. Teryaev, Fizika **B17**, 151 (2008), 0710.4211.

[12] M. Diehl and D. Y. Ivanov (2007), 0712.3533.

[13] M. V. Polyakov and C. Weiss, Phys.Rev. **D60**, 114017 (1999), hep-ph/9902451.

[14] O. B. Bylund, M. Defurne, and P. A. Guichon, Physical Review D **107** (2023), URL `https://doi.org/10.1103%2Fphysrevd.107.014020`.

[15] T. L. Collaboration (2014), URL `https://cds.cern.ch/record/1647400/files/LHCB-TDR-015.pdf`.

[16] A. A. et al., Journal of Instrumentation **8**, P05012 (2013), URL `https://doi.org/10.1088%2F1748-0221%2F8%2F05%2Fp05012`.

[17] A. Bravar, A. Buonaura, S. Corrodi, A. Damyanova, Y. Demets, L. Gerritzen, C. Grab, C. M. Perez, and A. Papa (2022), 2208.09906.

[18] Harada, Takeshi K., Ebata, K., Gogami, T., Hayakawa, S. H., Honda, R., Ichikawa, Y., Miwa, K., Nagae, T., Nanamura, T., Takahashi, T., et al., EPJ Web Conf. **271**, 03006 (2022), URL `https://doi.org/10.1051/epjconf/202227103006`.

[19] M. W. Mcnaughton et al. THE P C ANALYZING POWER BETWEEN 100-MEV AND 750-MEV. *Nucl. Instrum. Meth. A*, 241:435–440, 1985.

[20] B. Bonin et al. Measurement of the inclusive p-c analyzing power and cross section in the 1 gev

region and calibration of the new polarimeter pomme. *Nuclear Instruments and Methods in Physics Research Section A: Accelerators, Spectrometers, Detectors and Associated Equipment*, 288(2):379–388, 1990.

[21] E. Aprile-Giboni, R. Hausammann, E. Heer, R. Hess, C. Lechanoine-le Luc, W. Leo, S. Morenzoni, Y. Onel, and D. Rapin. Proton-carbon effective analyzing power between 95 and 570 mev. *Nuclear Instruments and Methods in Physics Research*, 215(1):147–157, 1983.